International Journal of Heat and Mass Transfer 55 (2012) 971–983

Contents lists available at SciVerse ScienceDirect

International Journal of Heat and Mass Transfer

journal homepage: www.elsevier.com/locate/ijhmt

Flow condensation in parallel micro-channels – Part 1: Experimental results and assessment of pressure drop correlations

Sung-Min Kim, Joseph Kim, Issam Mudawar *

Boiling and Two-Phase Flow Laboratory (BTPFL), and Purdue University International Electronic Cooling Alliance (PUIECA), Mechanical Engineering Building, 585 Purdue Mall, West Lafayette, IN 47907-2088, USA

ARTICLE INFO

Article history:
Received 10 March 2011
Received in revised form 26 July 2011
Accepted 26 July 2011
Available online 8 November 2011

Keywords:
Condensation
Micro-channel
High-flux

ABSTRACT

In this first part of a two-part study, experiments were performed to investigate condensation of FC-72 along parallel, square micro-channels with a hydraulic diameter of 1 mm and a length of 29.9 cm, which were formed in the top surface of a solid copper plate. The condensation was achieved by rejecting heat to a counter flow of water through channels brazed to the underside of the copper plate. The FC-72 entered the micro-channels slightly superheated, and operating conditions included FC-72 mass velocities of 68–367 kg/m^2 s, FC-72 saturation temperatures of 57.2–62.3 °C, and water mass flow rates of 3–6 g/s. Using high-speed video imaging and photomicrographic techniques, five distinct flow regimes were identified: smooth-annular, wavy-annular, transition, slug, and bubbly, with the smooth-annular and wavy-annular regimes being most prevalent. A detailed pressure model is presented which includes all components of pressure drop across the micro-channel. Different sub-models for the frictional and accelerational pressure gradients are examined using the homogenous equilibrium model (with different two-phase friction factor relations) as well as previous macro-channel and mini/micro-channel separated flow correlations. Unexpectedly, the homogenous flow model provided far more accurate predictions of pressure drop than the separated flow models. Among the separated flow models, better predictions were achieved with those for adiabatic and mini/micro-channels than those for flow boiling and macro-channels.

1. Introduction

Developments in many cutting-edge technologies are becoming increasingly dependent upon the ability to dissipate large amounts of heat from small surface areas. Examples include high performance computers, hybrid vehicle power electronics, lasers, radars and avionics. Although single-phase cooling systems have been successfully implemented in the past, the fast increase in power density in these technologies is pushing single-phase systems into unchartered territory in terms coolant flow rate and pressure drop, let alone the need to greatly increase heat transfer area. Even with these provisions, cooling goals in many applications are becoming virtually impossible to achieve with single-phase systems. Because of these inherent limitations, focus has shifted in recent years in favor of two-phase cooling schemes.

The superior cooling performance of two-phase cooling systems is realized by the enormous boiling and condensation heat transfer coefficients associated with heat acquisition from the heat-dissipating device and heat rejection, respectively. The quest for compact and lightweight packaging favors the use of miniature boiler designs, such as micro-channel heat sinks. While many present two-phase cooling systems employ fairly standard air-cooled condensers to reject the heat to the ambient, there is now a growing need for miniature condensers that can reject the heat by condensing a primary coolant in a compact primary cooling loop. The heat is transferred to a secondary liquid coolant and transported to a remote heat exchanger where is ultimately rejected to ambient air (or seawater for marine applications). Integrating miniature boilers and condensers in the compact primary cooling loop will necessitate greatly enhancing the condenser's performance to a level commensurate with that of the boiler. This goal can be realized with a condenser containing parallel micro-channels similar to those utilized in micro-channel flow boiling heat sinks. However, special care must be exercised to achieve the thermal goals without compromising the system's efficiency by the increased pressure drop.

Two-phase pressure drop is comprised of frictional as well as accelerational or decelerational components; acceleration is associated with boiling flows and deceleration condensing flows. In high-flux micro-channel boiling flows, acceleration contributes a

* Corresponding author. Tel.: +1 765 494 5705; fax: +1 765 494 0539.
E-mail address: mudawar@ecn.purdue.edu (I. Mudawar).
URL: https://engineering.purdue.edu/BTPFL (I. Mudawar).

0017-9310/$ - see front matter © 2011 Elsevier Ltd. All rights reserved.
doi:10.1016/j.ijheatmasstransfer.2011.10.013

Nomenclature

Bo	Bond number, $Bo = g(\rho_f - \rho_g)(D_h/2)^2/\sigma$
C	parameter in empirical correlations
C_c	contraction coefficient
c_p	specific heat at constant pressure
D	tube diameter
D_h	hydraulic diameter
F	Fanning friction factor
f_{app}	apparent friction factor
G	mass velocity
g	gravitational acceleration
H_b	distance between copper block's thermocouple planes
H_{ch}	micro-channel height
H_p	plenum height
H_t	distance between top thermocouple plane and base of micro-channel
h	enthalpy
h_{fg}	latent heat of vaporization
J	superficial velocity
k	thermal conductivity
L	length; micro-channel length
M	number of data points
MAE	mean absolute error
$\dot{m}$	mass flow rate
N	number of micro-channels in test module
P	pressure
P_{crit}	critical pressure
P_R	reduced pressure, $P_R = P/P_{crit}$
ΔP	pressure drop
q''_w	heat flux based on micro-channel's cooled perimeter
q''_{base}	heat flux based on total base area of micro-channel condenser
Re	Reynolds number
Su_g	Suratman number
T	temperature
v	specific volume
v_{fg}	specific volume difference between saturated vapor and saturated liquid
W_{ch}	micro-channel width
W_p	plenum width
W_s	width of solid wall separating micro-channels
We	Weber number
We^*	modified Weber number
X	Martinelli parameter
x	thermodynamic equilibrium quality
z	stream-wise coordinate

Greek symbols

α	void fraction
β	channel aspect ratio, W_{ch}/H_{ch}
δ	thickness of boundary layer
δ^+	dimensionless thickness of boundary layer, $\delta^+ = \delta/(D_h/2)$
μ	dynamic viscosity
ρ	density
$\bar{\rho}$	mixture density
σ	surface tension
σ_c	area ratio, $(W_{ch}H_{ch}N)/(W_pH_p)$
ϕ	two-phase pressure drop multiplier

Subscripts

A	accelerational
c	contraction
d	developing region
e	expansion
exp	experimental (measured)
F	frictional
f	saturated liquid; fully developed region
fo	liquid only
g	saturated vapor
go	vapor only
in	micro-channel inlet
out	micro-channel outlet
$pred$	predicted
sat	saturation
sp	single-phase
tot	total
tp	two-phase
tt	turbulent liquid-turbulent vapor
tv	turbulent liquid-laminar vapor
vt	laminar liquid-turbulent vapor
vv	laminar liquid-laminar vapor
w	wall; water

large fraction of the total pressure drop and, therefore, pumping power. However, in high-flux micro-channel condensing flows, deceleration provides the benefit of decreasing the pressure drop.

Another factor that influences pressure drop in condensing flows is two-phase flow regime. Condensing flow regimes in a tube can generally be classified into pure vapor, annular, slug, bubbly and pure liquid. The annular flow regime is the most crucial for condenser design since, for most practical designs, it prevails over the largest fraction of the tube length and provides very high heat transfer rates. The annular flow regime commences upstream in the tube once vapor begins to condense into a liquid film along the tube wall. This film is typically very thin and associated with a small thermal resistance between the vapor and the wall, resulting in very high heat transfer coefficients compared to the other flow regimes. As more of the vapor is condensed into liquid, the annular structure collapses and the slug and bubbly regimes are formed in succession.

The pursuit of compact condenser design is evident from several recent articles concerning multi-port micro-channel condensers. Yang and Web [1] investigated the condensation heat transfer characteristics of R12 along four parallel mini-channels with plain and micro-fin extruded tubes. Using R134a as working fluid, Yan and Lin [2], Wang et al. [3], and Koyama et al. [4] examined the performances of condensers having parallel micro-channels with hydraulic diameters of 2.0 mm, 1.46 mm, and 0.81 mm, respectively. Koyama et al. achieved the highest heat transfer coefficient, on the order of 10^4 W/m^2 K, in the high quality region with a relatively high mass velocity of $G = 652$ kg/m^2 s. Recently, Park and Hrnjak [5] examined the condensation of CO_2 in 0.89-mm circular parallel micro-channels and achieved maximum heat transfer coefficients on the same order as Koyama et al. with $G = 600$ kg/m^2 s.

While past studies have provided valuable databases for condensation in micro-channels, there is a general lack of fundamental understanding of interfacial behavior and shortage of predictive tools for both pressure drop and heat transfer coefficient. On the fundamental side, two key phenomena that are of great interest to modeling condensation in micro-channels are interfacial waves and turbulence in the annular liquid film. Past studies involving adiabatic, heated and evaporating liquid films have shown interfacial waves can greatly influence mass, momentum and heat transfer in the film [6–11]. Surface tension at the vapor-liquid interface

has been shown by Mudawar and El-Masri [12] to cause significant dampening of turbulent fluctuations in films, which can have a profound influence on heat transfer across the film. Aside from these fundamental issues, there is also a need for reliable correlations for condensing micro-channel flows. These issues and needs are the primary motivation for the present study.

This two-part study examines the two-phase flow regimes, pressure drop and heat transfer associated with condensation of FC-72 along parallel micro-channels with a hydraulic diameter of 1 mm. This first part will describe the construction of the condensation module, two-phase condensation loop and experimental methods used. High-speed video imaging and photomicrographic techniques are used to capture and classify two-phase flow regimes, which are compared to those from previous studies. The FC-72 pressure drop data are compared with the predictions of prior two-phase homogenous and separated flow models to identify most suitable models for micro-channel condensing flows. The second part of this study [13] will examine the heat transfer aspects of the condenser and provide a new correlation for micro-channel condensers.

2. Experimental methods

2.1. Condensation flow loop

Fig. 1(a) shows a schematic of the two-phase experimental apparatus constructed for this study. It uses two sub-loops, one for FC-72, the primary coolant, and the second for the cooling water. A 3M-company Fluorinet electronic liquid, FC-72 has excellent dielectric properties, a relatively moderate boiling point of 56 °C at 1 bar, and a surface tension much smaller than that of water, 0.0084 compared to 0.059 N/m at 1 bar. Table 1 provides a summary of the thermophysical properties of FC-72 at T_{sat} = 60 °C, which the saturation temperature corresponding an operating pressure close to that used in the present experiments.

Table 1
Thermophysical properties of FC-72 at T_{sat} = 60 °C.

h_{fg} (kJ/kg)	ρ_f (kg/m^3)	ρ_g (kg/m^3)	$\Re_f$ kg/m s	k_f (W/m K)	$c_{p,f}$ (kJ/kg K)	σ (mN/m)
93.7	1583.4	14.90	4.18×10^{-4}	0.0534	1.1072	8.0

The FC-72 is circulated through the primary loop with the aid of a gear pump. The fluid passes through a set of flow meters followed by an in-line electric heater, which is powered by a variable voltage transformer, before entering the micro-channel condensation module. Both temperature and pressure are measured in the inlet plenum of condensation module to determine fluid quality, which can be regulated to the desired value with the aid of a variable voltage transformer that powers the in-line heater upstream. The FC-72 condenses along the condensation module by rejecting heat to the waterside. The FC-72 temperature and pressure are measured once more at the condensation module's outlet plenum. Exiting the condenser module, the FC-72 is passed through a plate-type heat exchanger to condense any remaining vapor and achieve the desired temperature as the FC-72 returns to the primary loop's reservoir.

In the condensation module, water travels in a counter-flow direction to that of the FC-72. The water enters the condensation module at near room temperature and warms up by capturing heat from the condensing FC-72 flow. The warm water flows through a Lytron modular cooling system, where it cools back to near room

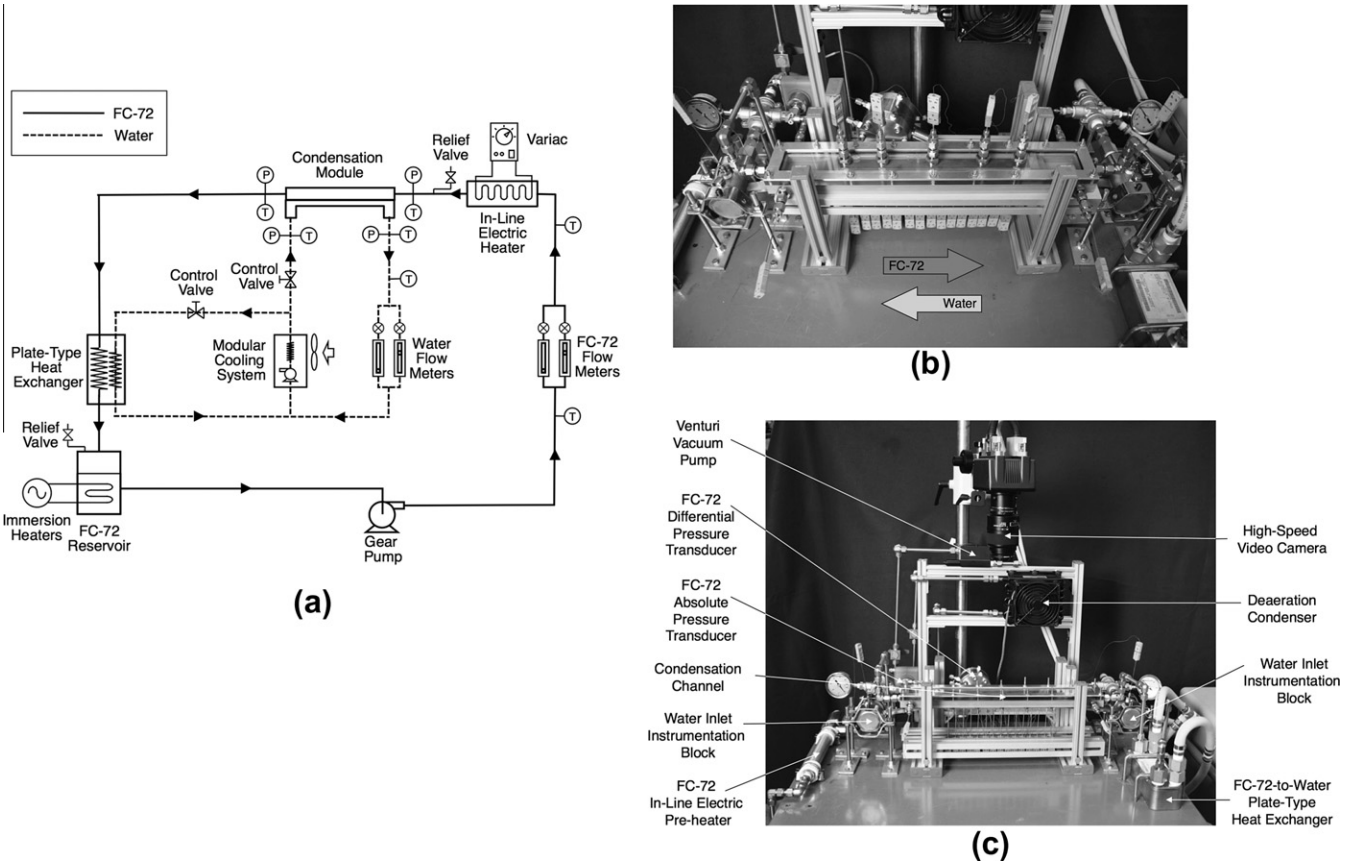

Fig. 1. (a) Schematic diagram of test loop, (b) photo of micro-channel condensation module, (c) photo of main part of test setup.

temperature. The water flow exiting the Lytron cooling system is divided into two parts, one flows back to the condensation module and the second to the plate-type heat exchanger. Fig. 1(b) and (c) show, respectively, a photo of the micro-channel condensation module and another of the main part of the experimental set-up.

2.2. Micro-channel condensation module

Fig 2(a) and (b) show the construction of micro-channel condensation module. The module consists of a cover plate, housing, condensation copper block, and water channels. The cover plate, which seals the tops of the square micro-channels, is made from transparent polycarbonate (Lexan) to facilitate photographic study of the condensing flow. The top of the oxygen-free copper block is 2-cm wide by 29.9-cm long, and contains ten of 1×1 mm^2 square micro-channels. Soldered to the underside of the copper block are three of 3.8×3.8 mm^2 brass tubes, which carry the counter flow of cooling water. Sixteen pairs of type-E thermocouples, which are embedded in the copper block beneath the micro-channels, run down the length of the copper block at 19 mm intervals. Using the assumption of one-dimensional heat conduction between the two thermocouple planes, both the heat flux and surface temperature at the base of the micro-channels may be determined along the stream-wise direction [14]. The dimensions of the test section are provided in Table 2.

The copper block is inserted into an insulating G-10 housing that features FC-72 inlet and outlet ports, micro-channel inlet and outlet plenums, and pressure and temperature measurement ports. The G-10 housing and water channels are covered by insulating layers of fiberglass.

2.3. Operating conditions and measurement accuracy

Experiments were performed to examine flow regimes and measure pressure drop and heat transfer coefficients corresponding to different flow rates of FC-72 and cooling water. The test matrix for the study consisted of 24 tests covering six FC-72 flow rates (G = 68, 118, 186, 248, 306, and 367 kg/m^2 s) and four coolant mass velocities (G_w = 69, 92, 115, and 138 kg/m^2 s).

Table 2
Test section dimensions.

W_{ch} (mm)	H_{ch} (mm)	W_s (mm)	H_t (mm)	H_b (mm)	L (cm)	N
1.0	1.0	1.0	9.65	7.62	29.9	10

Since the focus of this study is high-flux condensation, operating conditions were set to achieve mostly annular flow near the inlet of the micro-channels. Therefore, the FC-72 was introduced into the condensation module in pure vapor state with a thermodynamic equilibrium quality of 1.11–1.17 for low FC-72 flow rates (G = 68–186 kg/m^2 s) and 1.08–1.10 for high FC-72 flow rates (G = 248–367 kg/m^2 s). These conditions resulted in an upstream single-phase superheated vapor region 1.1–3.1 cm long (4–10% of the total channel length) for the low FC-72 flow rate range, and 2.7–5.8 cm long (9-19% of the total channel length) for the high FC-72 flow rate range. The inlet plenum pressure ranged from 1.040–1.324 bar. Operating conditions along the channel length were as follows: saturation temperatures of T_{sat} = 57.2–62.3 °C, qualities of x = 0–1.17, and heat fluxes of $q''_w = 0.43-3.21$ W/cm^2 .

There are several techniques for measuring liquid film thickness in two-phase applications [8,9,15]. Unfortunately, small channel size precludes the use of these techniques in the present application, causing a reliance on photographic methods instead. High-speed video imaging played a crucial role in capturing two-phase condensation flow regimes. Two key requirements for capturing the complex interfacial features in the micro-channels with high resolution are high shutter speed and high magnification. These goals were achieved with a Photron FASTCAM-Ultima camera capable of shutter speeds up to 1/120,000 s, which was used in conjunction with an assortment of Infinity K-2 lenses.

FC-72 pressure was measured in the inlet plenum with the aide of an absolute pressure transducer, while a differential pressure transducer measured pressure drop between the inlet and outlet plenums. Temperatures in the inlet and outlet plenums, copper

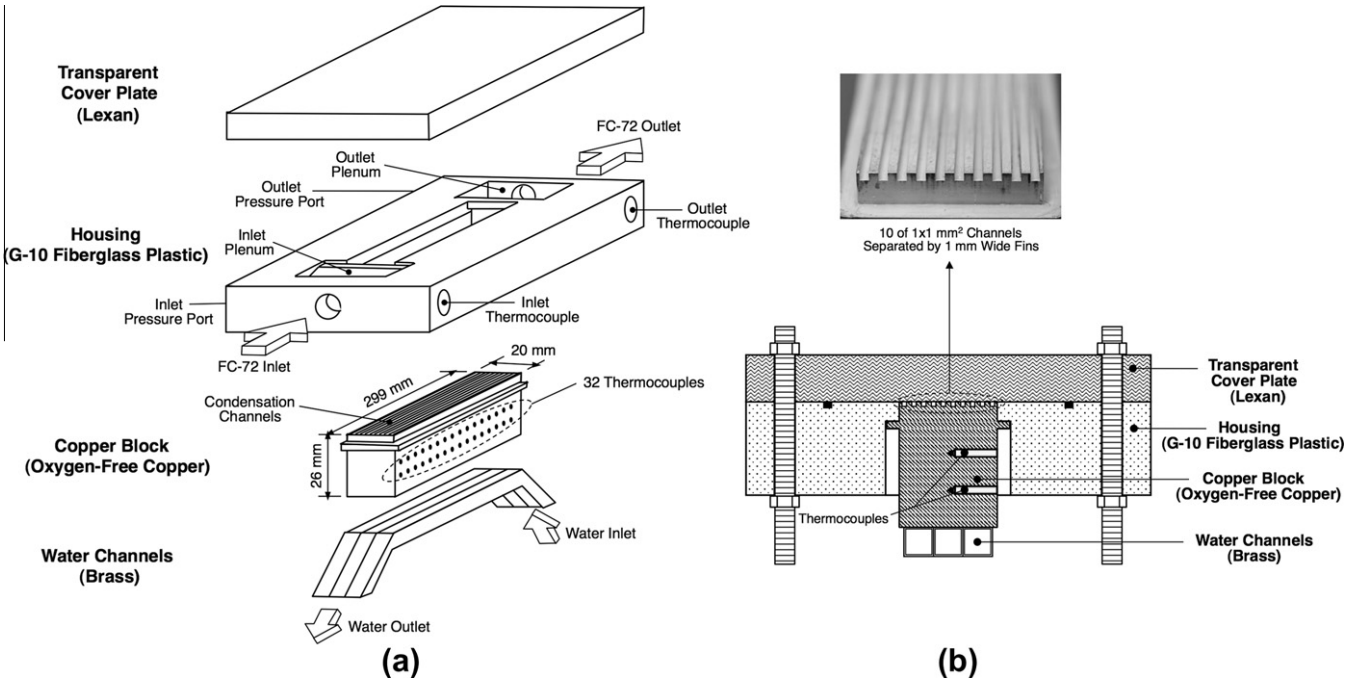

Fig. 2. (a) Construction and (b) cross-sectional view of micro-channel condensation module.

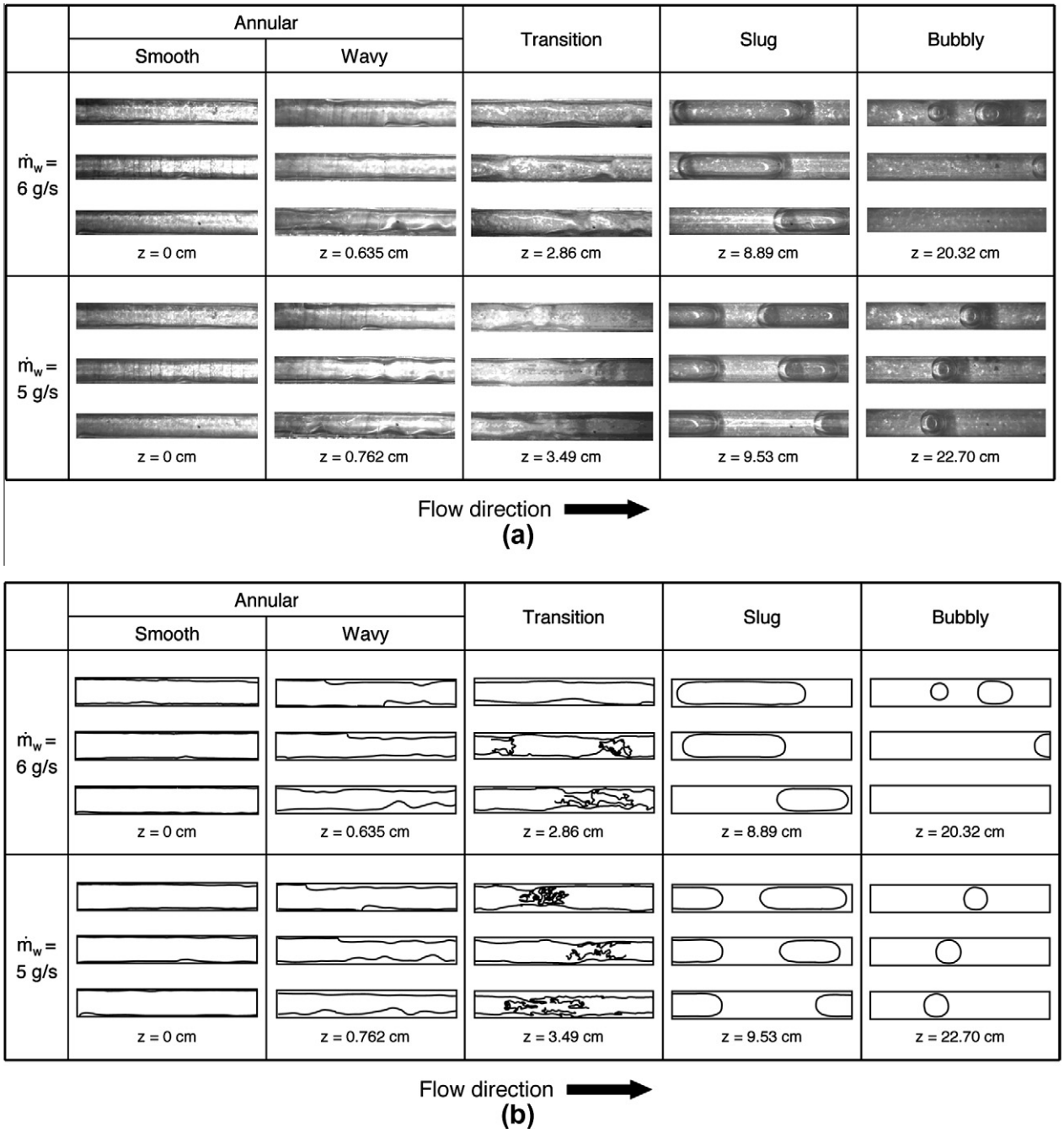

Fig. 3. Representative (a) photographs and (b) schematics of FC-72 condensation flow regimes in three adjacent channels for $G = 68$ kg/m^2 s.

block, and water channels were measured and processed by an HP-3852A data acquisition system. All measurements were made after all the system pressures and temperatures reached steady state.

Measurement uncertainties are ±0.5% for the pressure transducer and ±2.0% for the flow meter. Unlike the thermocouples inserted in the flow, the thermocouples embedded in the copper block are carefully calibrated using a procedure that brought down their uncertainties to less than ±0.03 °C. This is achieved by, first, carefully insulating the entire copper block and placing the block in an isothermal enclosure. This procedure is repeated for different enclosure temperatures. Thermocouples are typically off their mean value by ±0.03 °C, and this offset is corrected for the individual copper block thermocouples using a high accuracy HP data acquisition system. By using five thermocouple ports attached to top of the cover plate, heat loss through the cover plate is estimated at less than 2% of the heat input through the base of the micro-channels, which is calculated using the assumption of one-dimensional heat conduction between the two thermocouple planes. For a high mass velocity of $G = 367$ kg/m^2 s, the derived average uncertainties of base heat flux, vapor quality, and local heat transfer coefficient are ±4.6%, ±5.1%, and ±7.2%, respectively. For the worst case of a very low mass velocity of $G = 68$ kg/m^2 s, the average uncertainties of base heat flux, vapor quality, and local heat transfer coefficient are ±10.7%, ±11.0%, and ±16.1%, respectively.

3. Flow visualization results

High-speed video imaging and photomicrographic techniques were used to capture dominant condensation flow regimes along

the parallel micro-channels. Fig. 3 depicts representative flow regimes in three adjacent micro-channels channels at different locations from the micro-channel inlet. Five distinct flow regimes were identified. The *smooth-annular* flow regime is characterized by a very thin and fairly smooth liquid film that flows along the channel wall, with vapor flowing in the core clear of any liquid droplets. The film is barely discernible even when using a high magnification lens. This regime occurred in the inlet region of micro-channels under conditions of high inlet quality. The *wavy-annular* regime features a liquid film that is notably thicker that that of the smooth-annular regime, and having discernible interfacial waves. The next *transition* regime is characterized by bridging of liquid ligaments across the vapor care. The *slug* regime features elongated cylindrical bubbles whose length is several times larger than the width of the channel. The *bubbly* regime features spherical bubbles with a diameter approaching the of the micro-channel width. The bubbly regimes was least prevalent, observed only at the lowest tested mass velocity of $G = 68$ kg/m^2 s. Notice that no droplets are entrained in the vapor core for the smooth-annular and wavy-annular flows. This is in sharp contrast with annular flow associated with flow boiling in micro-channels. As observed by Qu and Mudawar [16], liquid droplets entrained in the vapor core have an appreciable influence on pressure drop and heat transfer in micro-channel boiling flows. This fundamental difference between micro-channel flow boiling and condensing flows and its implications to pressure drop prediction will be discussed later.

Fig. 4(a) shows the observed FC-72 flow regime transition data. Increasing the mass velocity is shown causing the smooth-annular regime, which corresponds to high quality values, to extend further downstream towards lower quality values, while narrowing the slug flow in the low quality region. Although the bubbly regime was observed in the present study for $G = 68$ kg/m^2 s, no bubbly regime data are shown in Fig. 4(a). This is due to the fact that the bubbly regime was observed for negative values of quality, indicating bubbles persisted in subcooled liquid flow due to thermodynamic non-equilibrium effects. Fig. 4(a) also compares the present FC-72 flow regime boundary data with flow regime boundary lines from Wang et al. [3] for R134a condensing flow inside a horizontal multi-port condenser featuring rectangular channels with a hydraulic diameter of 1.46 mm. Although no exact definitions were provided for their flow regimes, especially annular and wavy-annular, the boundary between the transition and slug regimes of the present study is in good agreement with that of Wang et al., however, the boundary between the wavy-annular and transition regimes corresponds to higher quality values than observed by Wang et al.

Fig. 4(b) compares the present FC-72 flow regime transition data with those of Triplett et al. [17] and Chung and Kawaji [18]. Triplett et al.'s data are based on air-water adiabatic flow in horizontal semi-triangular and circular micro-channels with hydraulic diameters of 1.09 and 1.097 mm, respectively. Chung and Kawaji conducted their experiments with an adiabatic mixture of nitrogen gas and water inside a 0.53-mm diameter horizontal circular tube. For all cases, the transition line to slug flow is observed when the superficial gas velocity is in a range of 1–4 m/s. The transition flow regime of this study was designated as slug-annular by both Triplett et al. and Chung and Kawaji, or 'serpentine-like gas core in churn flow' by Chung and Kawaji. The wavy-annular flow regime of this study had a thicker liquid film with waves having larger amplitude and wavelength than those of Triplett et al. and Chung and Kawaji, and is similar to the 'gas core with a wavy liquid film' regime designated as churn flow by Chung and Kawaji. Taking into consideration the differences in flow regime designation, the present flow regime boundaries are generally consistent with those from the two earlier studies.

Despite the fair agreement depicted in Fig. 4(a) and (b), it is important to emphasize the fundamental weaknesses of flow regime maps that utilize dimensional plots. The first is that the use of G versus x or J_f versus J_g may imply that such pairs of parameters govern all flow regimes, which is obviously not the case. The second weakness is the fact that flow regime boundaries are dominated by physical mechanisms and corresponding dimensionless groups that vary greatly from one boundary to another.

Fig. 4(c) shows an alternative presentation of flow regime boundaries in a dimensionless plot of modified Weber number, We^*, versus the Martinelli parameter, X_{tt}. Using the assumption that the inertia of the vapor phase is the dominant destructive force acting on the liquid film, while surface tension and liquid viscous forces are the stabilizing forces, Soliman [19] derived the following relations for modified Weber number by balancing the destructive and stabilizing forces.

$$We^* = 2.45\frac{Re_g^{0.64}}{Su_g^{0.3}(1+1.09X_{tt}^{0.039})^{0.4}} \quad \text{for} \quad Re_f \leqslant 1250 \tag{1a}$$

and

$$We^* = 0.85\frac{Re_g^{0.79}X_{tt}^{0.157}}{Su_g^{0.3}(1+1.09X_{tt}^{0.039})^{0.4}}\left[\left(\frac{\mu_g}{\mu_f}\right)^2\left(\frac{\upsilon_g}{\upsilon_f}\right)\right]^{0.084}$$
$$\text{for} \quad Re_f > 1250, \tag{1b}$$

where the Suratman number, Su_g, and Martinelli parameter (based on turbulent liquid-turbulent vapor) are given by

$$Su_g = \frac{\rho_g\sigma D}{\mu_g^2} \tag{2a}$$

and

$$X_{tt} = \left(\frac{\mu_f}{\mu_g}\right)^{0.1}\left(\frac{1-x}{x}\right)^{0.9}\left(\frac{\upsilon_f}{\upsilon_g}\right)^{0.5}, \tag{2b}$$

respectively [19]. Based on his own database, Soliman proposed that the flow is always annular for $We^* < 20$ and always mist for $We^* > 30$. While a few of the present smooth-annular flow regime data fall into Soliman's annular-to-mist transition region, most of the present data fall in Soliman's annular regime region. Fig. 6 also shows boundaries between annular, stratified-wavy, and plug regimes identified by Chen et al. [20] for condensation of R134a inside horizontal 12 and 14 mm diameter micro-finned tubes. Overall, there is general agreement with the present boundary lines between the wavy-annular and transition regimes, and between the transition and slug regimes. The second part of this study [13] will present new flow regime boundary lines for micro-channel condensing flows.

4. Pressure drop results

4.1. Experimental results

Fig. 5 shows the variation of total pressure drop measured between the inlet and outlet plenums of the condensation module with water mass velocity for different FC-72 mass velocities. Increasing the mass velocity of FC-72 increases the interfacial shear stress between the vapor core and liquid film due to the increasing vapor core velocity, which results in the measured increase in pressure drop. Fig. 5 shows the total pressure drop decreases slightly with increasing water mass velocity. This trend can be explained by the higher water flow rate increasing the wall heat flux, which hastens the flow deceleration leading to diminished interfacial shear.

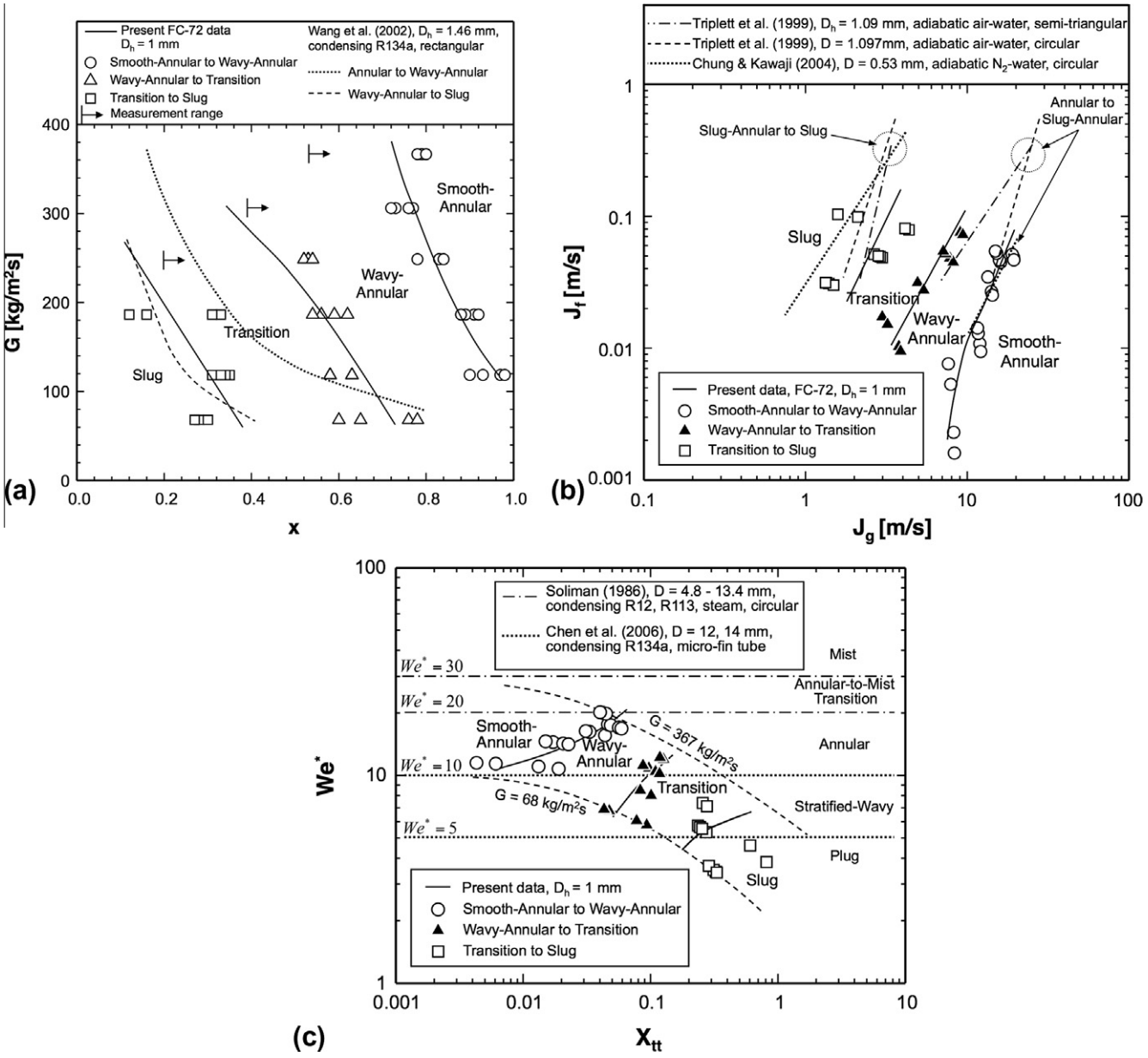

Fig. 4. Comparison of present FC-72 condensation flow regime data with those of (a) Wang et al. [3], (b) Triplett et al. [17] and Chung and Kawaji [18] and (c) comparison of present FC-72 condensation flow regime boundaries with those of Soliman [19] and Chen et al. [20].

4.2. Pressure drop components

For a superheated inlet condition, the total pressure drop between the upstream and downstream plenums can be obtained from

$$\Delta P_{tot} = \Delta P_c + \Delta P_{sp,d} + \Delta P_{tp} + \Delta P_{sp,f} + \Delta P_e. \tag{3}$$

The contraction pressure loss and expansion recovery at the inlet and outlet of the micro-channels, respectively, are determined from relations by Collier and Thome [21],

$$\Delta P_c = \frac{G^2 \upsilon_f}{2}\left[(\frac{1}{C_c} - 1)^2 + (1 - \sigma_c^2)\right]\left[1 + \frac{\upsilon_{fg} x_{e,in}}{\upsilon_f}\right], \tag{4a}$$

and

$$\Delta P_e = G^2 \sigma_c (\sigma_c - 1)\upsilon_f \left[1 + \frac{\upsilon_{fg} x_{e,out}}{\upsilon_f}\right]. \tag{4b}$$

For single-phase vapor flow at the plenum inlet, the contraction coefficient C_c due to the vena-contracta is obtained from a relation by Geiger [22],

$$C_c = 1 - \frac{1 - \sigma_c}{2.08(1 - \sigma_c) + 0.5371}. \tag{5}$$

For single-phase hydrodynamically developing vapor flow in the inlet region of the micro-channels, the pressure drop can be expressed as a function of the apparent friction factor,

$$\Delta P_{sp,d} = \frac{2 f_{app} G^2 L_{sp} \upsilon_g}{D_h}. \tag{6}$$

Since the FC-72 is introduced into the condensation module in superheated turbulent state with a Reynolds number range of 6000–31,000, the local pressure is predicted according to Zhi-qing's [23] analytical solution for turbulent developing vapor flow in a circular tube,

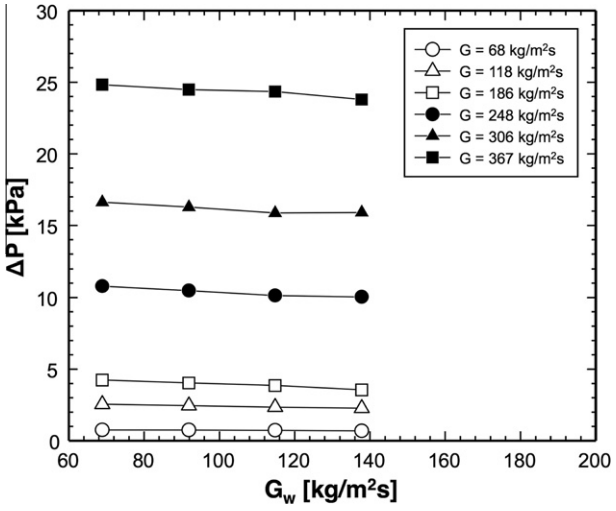

Fig. 5. Variation of measured total pressure drop with water mass velocity for different FC-72 mass velocities.

$$L_{sp}/D_h = 1.4039 Re_{sp}^{0.25} \delta^{+1.25} \left(1 + 0.1577\delta^{+} - 0.1793\delta^{+2} - 0.0168\delta^{+3} + 0.0064\delta^{+4}\right), \quad (7)$$

where

$$f_{app} = \left[\frac{1}{(1 - 0.25\delta^{+} + 0.0667\delta^{+2})^2} - 1\right] \frac{0.25}{L_{sp}/D_h} \quad \text{for} \quad \delta^{+} < 1 \quad \text{(developing region)} \quad (8a)$$

and

$$f_{app} = \left(0.07 + 0.316 \frac{L_{sp}/D_h}{Re_{sp}^{0.25}}\right) \frac{0.25}{L_{sp}/D_h} \quad \text{for} \quad \delta^{+} = 1 \quad \text{(fully-developed region)}. \quad (8b)$$

When the FC-72 completely condenses to pure liquid in the downstream region of the micro-channel, the pressure drop for the single-phase liquid region, where the flow is assumed fully-developed, can be determined from [24,25]

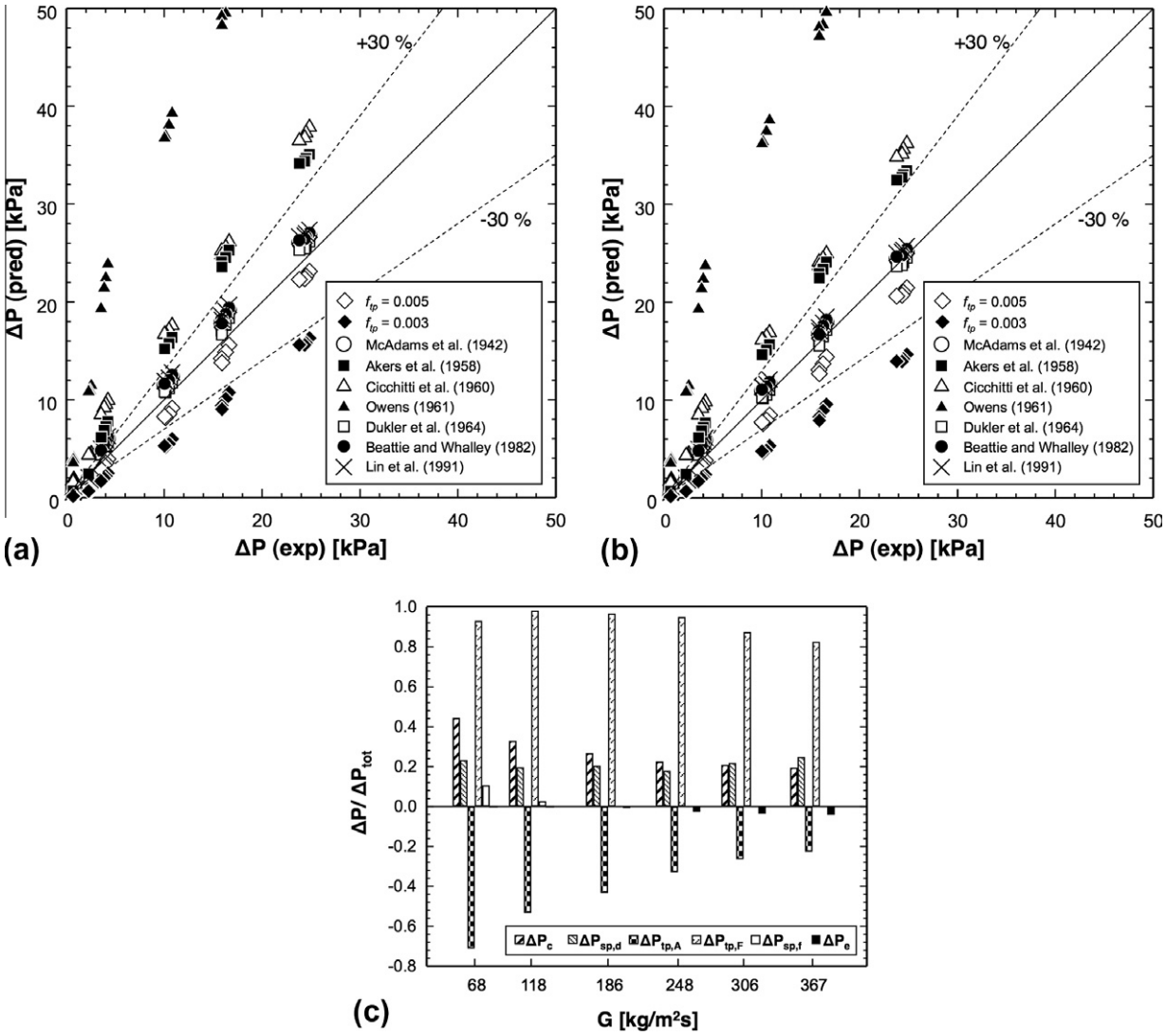

Fig. 6. Comparison of present FC-72 pressure drop data with predictions of (a) homogeneous equilibrium model, and (b) homogeneous equilibrium model with accelerational pressure drop based on separated flow model and Zivi's [26] relation for void fraction. (c) Contributions of individual components of pressure drop to total pressure drop for different mass velocities and G_w = 69 kg/m^2 s predicted with the frictional pressure gradient determined by the homogenous equilibrium model using the viscosity model of Dukler et al. [36], and the accelerational pressure gradient determined by the separated flow model using Zivi's relation for void fraction.

Table 3
Homogeneous equilibrium model for two-phase frictional pressure gradient, and corresponding MAE in predicting present total pressure drop data.

$\left(\frac{dP}{dz}\right)_F = -\frac{2}{D_h} f_{tp} \bar{\rho} u^2 = -\frac{2}{D_h} f_{tp} \upsilon_f G^2 \left(1 + x \frac{\upsilon_{fg}}{\upsilon_f}\right)$

Constant friction factor method

Author(s)	Applications	f_{tp}	MAE [%]
Lewis and Robertson [27], Markson et al. [28]	High pressure steam-water boilers	0.005	31.72
Bottomley [29], Benjamin and Miller [30], Allen [31]	Low pressure flashing steam-water flows	0.003	56.77

Two-phase mixture viscosity method

$f_{tp} Re_{tp} = 24(1 - 1.3553\beta + 1.9467\beta^2 - 1.7012\beta^3 + 0.9564\beta^4 - 0.2537\beta^5)$ for $Re_{tp} < 2000$

$f_{tp} = 0.079 Re_{tp}^{-0.25}$ for $2000 \leqslant Re_{tp} < 20,000$

$f_{tp} = 0.046 Re_{tp}^{-0.2}$ for $Re_{tp} \geqslant 20,000$, where $Re_{tp} = \frac{GD_h}{\mu_{tp}}$

Author(s)	Equation	MAE [%]
McAdams et al. [32]	$\frac{1}{\mu_{tp}} = \frac{x}{\mu_g} + \frac{1-x}{\mu_f}$	17.22
Akers et al. [33]	$\mu_{tp} = \frac{\mu_f}{[(1-x)+x(\frac{\upsilon_g}{\upsilon_f})^{0.5}]}$	34.98
Cicchitti et al. [34]	$\mu_{tp} = x\mu_g + (1-x)\mu_f$	85.16
Owens [35]	$\mu_{tp} = \mu_f$	306.0
Dukler et al. [36]	$\mu_{tp} = \frac{x\upsilon_g\mu_g + (1-x)\upsilon_f\mu_f}{x\upsilon_g + (1-x)\upsilon_f}$	15.92
Beattie and Whalley [37]	$\mu_{tp} = \omega\mu_g + (1-\omega)(1+2.5\omega)\mu_f$, $\omega = \frac{x\upsilon_g}{\upsilon_f + x\upsilon_{fg}}$	17.34
Lin et al. [38]	$\mu_{tp} = \frac{\mu_f\mu_g}{\mu_g + x^{1.4}(\mu_f - \mu_g)}$	17.05

$$\Delta P_{sp,f} = \frac{2 f_{sp,f} G^2 L_{sp,f} \upsilon_f}{D_h}, \tag{9}$$

where

$$f_{sp,f} Re_{sp,f} = 24(1 - 1.3553\beta + 1.9467\beta^2 - 1.7012\beta^3 + 0.9564\beta^4 - 0.2537\beta^5) \quad \text{for} \quad Re_{sp,f} < 2000, \tag{10a}$$

$$f_{sp,f} = 0.079 Re_{sp,f}^{-0.25} \quad \text{for} \quad 2000 \leqslant Re_{sp,f} < 20,000 \tag{10b}$$

and

$$f_{sp,f} = 0.046 Re_{sp,f}^{-0.2} \quad \text{for} \quad Re_{sp,f} \geqslant 20,000. \tag{10c}$$

For the two-phase region, the pressure drop consists of accelerational and frictional components,

$$\Delta P_{tp} = \Delta P_{tp,A} + \Delta P_{tp,F}. \tag{11}$$

For a constant mass velocity, the differential form of accelerational two-phase pressure drop can be expressed as

$$-\left(\frac{dP}{dz}\right)_A = G^2 \frac{d}{dz}\left[\frac{\upsilon_g x^2}{\alpha} + \frac{\upsilon_f (1-x)^2}{(1-\alpha)}\right], \tag{12}$$

where the void fraction can be obtained from Zivi's [26] correlation

$$\alpha = \left[1 + \left(\frac{1-x}{x}\right)\left(\frac{\upsilon_f}{\upsilon_g}\right)^{2/3}\right]^{-1}. \tag{13}$$

For the homogeneous equilibrium model, the void fraction is related to thermodynamic equilibrium quality by the relation

$$\alpha = \left[1 + \left(\frac{1-x}{x}\right)\left(\frac{\upsilon_f}{\upsilon_g}\right)\right]^{-1}. \tag{14}$$

Substituting the above relation in Eq. (12) while neglecting property changes yields the following widely used form of accelerational two-phase pressure gradient for the homogeneous equilibrium model,

$$-\left(\frac{dP}{dz}\right)_A = G^2 \upsilon_{fg} \frac{dx}{dz}. \tag{15}$$

The accelerational two-phase pressure drop can be determined by integrating Eqs. (12) and (15) numerically along the streamwise direction,

$$\Delta P_{tp,A} = \int_0^{L_{tp}} -\left(\frac{dP}{dz}\right)_A dz. \tag{16}$$

When determining the total pressure drop via the homogeneous equilibrium models, both the simple and general forms of accelerational pressure drop, Eqs. (15) and (12), respectively, will be examined. In case of separated flow models, only the general form of accelerational pressure gradient, Eq. (12), will be used to determine the accelerational pressure drop.

The frictional two-phase pressure drop can be determined by integrating the relation for frictional pressure gradient corresponding to the chosen model or correlation as indicated in Tables 3–5,

$$\Delta P_{tp,F} = \int_0^{L_{tp}} -\left(\frac{dP}{dz}\right)_F dz. \tag{17}$$

In the two-phase condensing region, the local saturation temperature of FC-72 is obtained from the local saturation pressure, and the thermophysical properties for liquid and vapor are based on local saturation pressure.

4.3. Comparison with different pressure drop models and correlations

To determine the two-phase frictional pressure drop, both homogeneous equilibrium and separated flow models are considered.

4.3.1. Homogeneous equilibrium model (HEM)

Both constant friction factor [27–31] and two-phase mixture viscosity [32–38] methods are used to predict the two-phase frictional pressure gradient via the homogeneous equilibrium model. In order to check the sensitivity of different accelerational pressure drop relations to total pressure drop, both the simple and general forms of accelerational pressure drop, Eqs. (15) and (12), respectively, are compared. Fig. 6(a) and (b) compare the present FC-72 pressure drop data to predictions based on two different constant friction factors, f_{tp} = 0.003 and 0.005, and seven different two-phase viscosity models. The total pressure drop in Fig. 6(a) is based entirely on the homogeneous equilibrium model (i.e., using Eq. (15) for the accelerational pressure gradient), while the accelerational pressure gradient in Fig. 6(b) is based on Eq. (12) and Zivi's relation for void fraction. Comparing Fig. 6(a) and (b) shows the former approach only slightly overpredicts the data

Table 4
Two-phase frictional pressure gradient correlations for macro-channels based on the separated flow model, and corresponding MAE in predicting present total pressure drop data.

Author(s)	Equation	Remarks	MAE [%]
Lockhart and artinelli [39]	$\left(\frac{dP}{dz}\right)_F = \left(\frac{dP}{dz}\right)_f \phi_f^2,\ \phi_f^2 = 1 + \frac{C}{X} + \frac{1}{X^2},\ X^2 = \frac{(dP/dz)_f}{(dP/dz)_g}$ $C_{vv} = 5,\ C_{tv} = 10,\ C_{vt} = 12,\ C_{tt} = 20$	D_h = 1.49–25.83 mm adiabatic fluids: water, oils, hydrocarbons	80.26
Friedel [40]	$\left(\frac{dP}{dz}\right)_F = \left(\frac{dP}{dz}\right)_{fo} \phi_{fo}^2$ $\phi_{fo}^2 = (1-x)^2 + x^2\left(\frac{\upsilon_g}{\upsilon_f}\right)\left(\frac{f_{go}}{f_{fo}}\right) + \cdots + 3.24x^{0.78}(1-x)^{0.224}\left(\frac{\upsilon_g}{\upsilon_f}\right)^{0.91}\left(\frac{\mu_g}{\mu_f}\right)^{0.19}\left(1-\frac{\mu_g}{\mu_f}\right)^{0.7} Fr_{tp}^{-0.045} We_{tp}^{-0.035}$ $Fr_{tp} = \frac{G^2}{gD_h\rho_H^2},\ We_{tp} = \frac{G^2 D_h}{\sigma\rho_H},\ \rho_H = \frac{1}{x\upsilon_g + (1-x)\upsilon_f}$	D > 4 mm Fluids: air/water, air/oil, R12 (25000 data points)	173.4
Chisholm [41]	$\left(\frac{dP}{dz}\right)_F = \left(\frac{dP}{dz}\right)_{fo} \phi_{fo}^2$ $\phi_{fo}^2 = 1 + (\Gamma^2 - 1)\left[Bx^{0.875}(1-x)^{0.875} + x^{1.75}\right]$ $\Gamma^2 = \frac{(dP/dz)_{go}}{(dP/dz)_{fo}}$, for B values refer to Chisholm [41]	Flow boiling Fluids: air/water, steam	114.1
Muller-Steinhagen and Heck [42]	$\left(\frac{dP}{dz}\right)_F = \left\{\left(\frac{dP}{dz}\right)_{fo} + 2\left[\left(\frac{dP}{dz}\right)_{go} - \left(\frac{dP}{dz}\right)_{fo}\right]x\right\}(1-x)^{1/3} + \left(\frac{dP}{dz}\right)_{go} x^3$	D = 4–392 mm Fluids: air/water, water, hydrocarbons, refrigerants (9300 data points)	54.88
Jung and Radermacher [43]	$\left(\frac{dP}{dz}\right)_F = \left(\frac{dP}{dz}\right)_{fo} \phi_{fo}^2,\ \phi_{fo}^2 = 12.82 X_{tt}^{-1.47}(1-x)^{1.8}$ $X_{tt} = \left(\frac{\mu_f}{\mu_g}\right)^{0.1}\left(\frac{1-x}{x}\right)^{0.9}\left(\frac{\upsilon_f}{\upsilon_g}\right)^{0.5}$	D = 9.1 mm Annular flow boiling Fluids: pure and mixtures of R22, R114, R12, R152a	288.3
Wang et al. [44]	For $G \geqslant 200$ kg/m^2 s, $\left(\frac{dP}{dz}\right)_F = \left(\frac{dP}{dz}\right)_g \phi_g^2,\ \phi_g^2 = 1 + 9.4X^{0.62} + 0.564X^{2.45}$ For $G < 200$ kg/m^2 s, $\left(\frac{dP}{dz}\right)_F = \left(\frac{dP}{dz}\right)_f \phi_f^2, \phi_f^2 = 1 + \frac{C}{X} + \frac{1}{X^2}$, $C = 4.566 \times 10^{-6} X^{0.128} Re_{fo}^{0.938}\left(\frac{\upsilon_f}{\upsilon_g}\right)^{2.15}\left(\frac{\mu_f}{\mu_g}\right)^{5.1}$	D = 6.5 mm adiabatic fluids: R22, R134a, R407C	86.19
Cavallini et al. [45]	$\left(\frac{dP}{dz}\right)_F = \left(\frac{dP}{dz}\right)_{fo} \phi_{fo}^2$ For $j_g^* \geqslant 2.5$, $\phi_{fo}^2 = (1-x)^2 + x^2\left(\frac{\upsilon_g}{\upsilon_f}\right)\left(\frac{f_{go}}{f_{fo}}\right) + \cdots + 1.262x^{0.6978}\left(\frac{\upsilon_g}{\upsilon_f}\right)^{0.3278}\left(\frac{\mu_g}{\mu_f}\right)^{-1.181}\left(1-\frac{\mu_g}{\mu_f}\right)^{3.477} We_{go}^{-0.1458}$ For $j_g^* < 2.5,\ \phi_{fo}^2 = \phi_{fo,Friedel}^2$ $We_{go} = \frac{G^2 D_h}{\rho_g \sigma},\ j_g^* = \frac{Gx}{\rho_g}\sqrt{\frac{\rho_g}{(\rho_f - \rho_g)gD_h}}$	D > 3.1 mm Condensation Fluids: R22, R134a, R125, R32, R236ea, R407c, R410A	597.8

compared to the latter. Therefore, the differences in predictions of total pressure drop in Fig. 8(a) and (b) are due mostly to the different frictional pressure drop models used.

Given the slightly better predictions in Fig. 6(b) compared to Fig. 6(a), all subsequent accelerational pressure drop calculations in Figs. 6(c) and 7(a) and (b) will be based on the general form of accelerational pressure drop, Eq. (12), using Zivi's void fraction relation.

Table 3 provides details of the constant two-phase friction factor and two-phase viscosity methods as well as their accuracy in predicting the present data. The accuracy of individual models is measured by mean absolute error, which is defined as

$$MAE = \frac{1}{M}\sum \frac{|\Delta P_{\text{pred}} - \Delta P_{exp}|}{\Delta P_{exp}} \times 100\%. \tag{18}$$

In general, the homogeneous equilibrium model is better suited to dispersed two-phase flows such as bubbly flow. The fundamental premises of this model fall apart for regimes involving separation between the liquid and vapor phases or large velocity differences between the two phases. Annular flow is an example of a regime where the use of the homogenous equilibrium model is generally avoided. In spite of the fact that annular flow was dominant throughout the present measurement, Fig. 6(a) and (b) prove that, when used in conjunction with most two-phase viscosity models, excepting those of Cicchitti et al. [34] and Owens [35], the homogeneous equilibrium model provides fairly accurate predictions of the present experimental data. Most notably, the viscosity model by Dukler et al. [36], with a MAE of 15.92%, provides the best predictions among all viscosity relations. In fact, this model provides better accuracy than all separated flow correlations as discussed in the next section.

Fig. 6(c) shows the contributions of individual pressure drop components to total pressure drop using the mixture viscosity model by Dukler et al. For a condensing flow, the accelerational two-phase pressure drop term is negative because of the deceleration along the stream-wise direction. In fact, condensation reduces two-phase pressure drop, as opposed to flow boiling, where two-phase pressure drop is increased by the stream-wise acceleration, and the accelerational pressure drop is positive. Fig. 6(c) shows that the magnitude of ΔP_{tot} is dictated mostly by two-phase friction and acceleration. Increasing the mass velocity decreases the magnitude of $\Delta P_{tp,A}/\Delta P_{tot}$ because of the decreasing amount of vapor being condensed. The contributions of $\Delta P_{sp,f}$ and ΔP_e to ΔP_{tot} are minimal, while those of ΔP_c and $\Delta P_{sp,d}$ are more significant because of the pure vapor state at the micro-channel inlet.

4.3.2. Separated flow models (SFMs)

Tables 4 and 5 provide a select summary of separated flow frictional pressure drop correlations that have been recommended for macro-channels [39–45] and mini/micro-channels [46–54], respectively. These include a mix of correlations for flow boiling and condensation, adiabatic, flow boiling and condensing flows, and for isolated tubes and multi-channel heat sinks. Notice that the correlation of Jung and Radermacher [43] is based on the assumption of $\Delta P_{tp} \approx \Delta P_f$ because the accelerational component was found to be small in their flow boiling experiments.

Fig. 7(a) shows that all seven macro-channel correlations overpredict the present FC-72 condensation data. Notably, the total pressure drop is highly overpredicted by the correlations of Friedel [40], Chisholm [41], Jung and Radermacher [43], and Cavallini et al. [45], with corresponding MAE values of 173.42%, 114.06%, 288.27%, and 597.75%, respectively.

Fig. 7(b) compares the present FC-72 micro-channel condensation pressure drop data with predictions using separated flow correlations for frictional pressure drop in mini/micro-channels. The correlations of Mishima and Hibiki [46], Lee and Lee [48],

Table 5
Two-phase frictional pressure gradient correlation for mini/micro-channels based on the separated flow model, and corresponding MAE in predicting present total pressure drop data.

Author(s)	Equation	Remarks	MAE [%]
Mishima and Hibiki [46]	$(\frac{dP}{dz})_F = (\frac{dP}{dz})_f \phi_f^2, \phi_f^2 = 1 + \frac{C}{X} + \frac{1}{X^2}$ $C = 21[1 - \exp(-0.319Dh)]; D_h$ [mm]	D = 1.05–4.08 mm adiabatic fluid: air/water	27.15
Tran et al. [47]	$(\frac{dP}{dz})_F = (\frac{dP}{dz})_{fo} \phi_{fo}^2$ $\phi_{fo}^2 = 1 + (4.3I^{-2} - 1)[N_{conf} x^{0.875}(1-x)^{0.875} + x^{1.75}]$ $N_{conf} = \sqrt{\frac{\sigma}{g(\rho_f - \rho_g)D_h^2}}$	D_h = 2.40, 2.46, 2.92 mm Flow boiling Fluids: R134a, R12, R113	276.1
Lee and Lee [48]	$(\frac{dP}{dz})_F = (\frac{dP}{dz})_f \phi_f^2, \quad \phi_f^2 = 1 + \frac{C}{X} + \frac{1}{X^2}$ $C_{vv} = 6.833 \times 10^{-8} \lambda^{-1.317} \psi^{0.719} Re_{fo}^{0.557}, \; C_{tv} = 3.627 Re_{fo}^{0.174}$ $C_{vt} = 6.185 \times 10^{-2} Re_{fo}^{0.726}, \; C_{tt} = 0.048 Re_{fo}^{0.451}$ $\psi = \frac{\mu_f j_f}{\sigma}, \; \lambda = \frac{\mu_f^2}{\rho_f \sigma D_h}$	D_h = 0.78–6.67 mm adiabatic fluid: air/water	36.26
Zhang and Webb [49]	$(\frac{dP}{dz})_F = (\frac{dP}{dz})_{fo} \phi_{fo}^2$ $\phi_{fo}^2 = (1-x)^2 + 2.87x^2 P_R^{-1} + 1.68x^{0.8}(1-x)^{0.25} P_R^{-1.64}$, $P_R = P/P_{crit}$	D = 0.96–6.20 mm adiabatic multi-channel fluids: R134a, R22, R404a	522.9
Chen et al. [50]	$(\frac{dP}{dz})_F = (\frac{dP}{dz})_{fo,Friedel} \Omega$ For $Bo < 2.5, \; \Omega = \frac{0.0333 Re_{fo}^{0.45}}{Re_g^{0.09}(1+0.4e^{-Bo})}$ For $Bo \geqslant 2.5, \; \Omega = \frac{We_{fo}^{0.2}}{(2.5+0.06Bo)}, \; Bo = g(\rho_f - \rho_g)\frac{(D_h/2)^2}{\sigma}$	D = 1.02–9 mm adiabatic fluids: air/water, R410A, ammonia	47.65
Yu et al. [51]	$(\frac{dP}{dz})_F = (\frac{dP}{dz})_f \phi_f^2, \phi_f^2 = \frac{1}{X_{vt}^{1.9}}$, $X_{vt} = 18.65(\frac{v_f}{v_g})^{0.5}(\frac{1-x}{x})\frac{Re_g^{0.1}}{Re_f^{0.5}}$	D = 2.98 mm Flow boiling Fluids: water, ethylene glycol, aqueous mixtures of ethylene glycol	51.25
Nino et al. [52]	$(\frac{dP}{dz})_F = (\frac{dP}{dz})_{go} \phi_{go}^2$ $\phi_{go}^2 = exp(-0.046X_{ann}) + 0.22[exp(-0.002X_{ann}) - exp(-7X_{ann})]$ $X_{ann} = [(X_{tt} + \frac{1}{We_g^{1.3}})(\frac{v_g}{v_f})^{0.9}], \; We_g = \frac{(Gx)^2 D_h}{\sigma \rho_g}$ $X_{tt} = \left(\frac{\mu_f}{\mu_g}\right)^{0.125}\left(\frac{1-x}{x}\right)^{0.875}\left(\frac{v_f}{v_g}\right)^{0.5}$	D_h = 1.02, 1.54 mm adiabatic multi-channel fluids: R410A, R134a, air/water	34.24
Lee and Mudawar [53]	$(\frac{dP}{dz})_F = (\frac{dP}{dz})_f \phi_f^2, \; \phi_f^2 = 1 + \frac{C}{X} + \frac{1}{X^2}$ $C_{vv} = 2.16 Re_{fo}^{0.047} We_{fo}^{0.60}, \; C_{vt} = 1.45 Re_{fo}^{0.25} We_{fo}^{0.23}$, $We_{fo} = \frac{G^2 D_h}{\sigma \rho_f}$	D_h = 0.349 mm Flow boiling Multi-channel Fluids: R134a, water	57.55
Hwang and Kim [54]	$(\frac{dP}{dz})_F = (\frac{dP}{dz})_f \phi_f^2, \; \phi_f^2 = 1 + \frac{C}{X} + \frac{1}{X^2}$, $C = 0.227 Re_{fo}^{0.452} X^{-0.32} N_{conf}^{-0.82}$	D = 0.244, 0.430, 0.792 mm adiabatic fluid: R134a	53.95

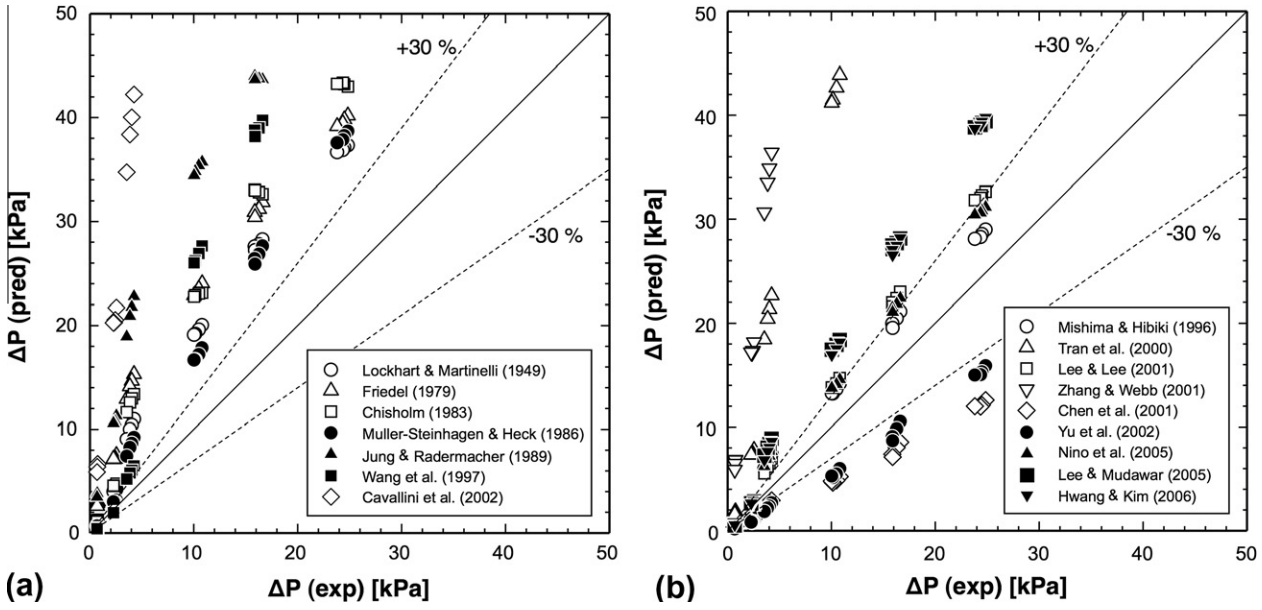

Fig. 7. Comparison of present FC-72 pressure drop data with predictions of separated flow correlations recommended for (a) macro-channels and (b) mini/micro-channels.

and Nino et al. [52], which are all based on adiabatic air-water flow, provide fair predictions of the present data, with MAE values of 27.15%, 36.26%, and 34.24%, respectively. The correlations of Lee and Mudawar [53] and Tran et al. [47], which are based on micro-channel flow boiling, overpredict the present data with a MAE of 57.55% and 276.1%, respectively. The large MAE of 522.86% for

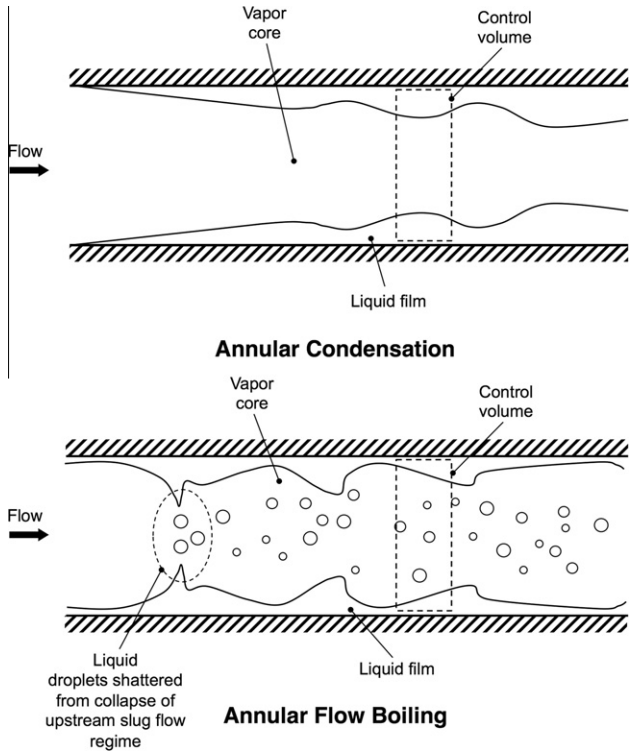

Fig. 8. Fundamental differences between annular condensation and annular flow boiling in micro-channels.

the Zhang and Webb correlation [49] may be attributed to the relatively low reduced pressure range of the present FC-72 data, $P_R = 0.05–0.07$, compared to the recommended range of $P_R > 0.2$ for the original correlation.

By closely examining the predictive accuracy of the separated mini/micro-channels flow correlations, it can be concluded that, even on a local basis, condensation behavior is fundamentally different from that of flow boiling and perhaps closer to that of adiabatic two-phase flow. One obvious difference between flow boiling on one hand, and condensing and adiabatic two-phase flows on the other, is the relative abundance of entrained droplet in the former and absence from the latter two, as schematically shown in Fig. 8. This phenomenon is especially important for mini/micro-channel flows, where the annular regime is dominant regardless of heating conditions. As indicated by Qu and Mudawar [16], the transition to the annular regime in flow boiling occurs far upstream in a micro-channel, but with an abundance of entrained droplets that are formed by shattering of liquid from the micro-channel's upstream. However, the flow visualization results of the present study show no droplets are formed in the annular regions of the micro-channel. This conclusion highlights the need for new models and correlations that can accurately predict condensation behavior in mini/micro-channels, especially when implemented in a multi-channel configuration.

5. Conclusions

This study concerns transport phenomena associated with condensation in micro-channels. This first part of the study discussed the construction of the condensation module and flow loop, and the experimental methods used. High-speed video and photomicrographic techniques were used to explore and help categorize two-phase flow regimes associated with condensation of FC-72 in parallel square channels with $D_h = 1$ mm. The total pressure drop measured between the inlet and outlet plenums was compared to predictions of previous models based on homogenous equilibrium and separated flow models. Key findings from this study are as follows:

(1) Five dominant condensation regimes, smooth-annular, wavy-annular, transition, slug, and bubbly, are identified. Transitions between these regimes are in general agreement with those from previous studies.
(2) The total pressure drop increases with increasing mass velocity due largely to the increased interfacial shear stress between the vapor core and the annular liquid film. Increasing the flow rate of cooling water decreases the total pressure drop slightly because of increased flow deceleration.
(3) A complete model was constructed for total pressure drop between the inlet and outlet plenums. To calculate the two-phase frictional pressure drop portion of the total pressure drop, different homogenous and separated models were tested. Although annular flow was dominant throughout the present experiments, most homogeneous models unexpectedly provided accurate predictions of the present data. All separated flow macro-channel correlations overpredicted the experimental data, some with very large MAE. Among the separated flow mini/micro-channels correlations, those that are based on adiabatic and condensing two-phase flows provide better predictions than those based on flow boiling. This can be attributed to fundamental differences in local annular flow behavior between condensing and adiabatic flows on one hand and evaporating flows on the other. While entrained droplets play an important role in evaporating flows, no droplets were observed in the present condensation experiments. Overall, weak predictions of separated flow correlations highlight the need of further study and new predictive tools specifically tailored to micro-channel condensing flows.

Acknowledgement

The authors are grateful for the support of the Office of Naval Research (ONR) for this study.

References

[1] C.-Y. Yang, R.L. Webb, Condensation of R-12 in small hydraulic diameter extruded aluminum tubes with and without micro-fins, Int. J. Heat Mass Transfer 39 (1996) 791–800.
[2] Y.-Y. Yan, T.-F. Lin, Condensation heat transfer and pressure drop of refrigerant R-134a in a small pipe, Int. J. Heat Mass Transfer 42 (1999) 697–708.
[3] W.-W. Wang, T.D. Radcliff, R.N. Christensen, A condensation heat transfer correlation for millimeter-scale tubing with flow regime transition, Exp. Thermal Fluid Sci. 26 (2002) 473–485.
[4] S. Koyama, K. Kuwahara, K. Nakashita, K. Yamamoto, An experimental study on condensation of refrigerant R134a in a multi-port extruded tube, Int. J. Refrigeration 24 (2003) 425–432.
[5] C.Y. Park, P. Hrnjak, CO_2 flow condensation heat transfer and pressure drop in multi-port microchannels at low temperatures, Int. J. Refrigeration 32 (2009) 1129–1139.
[6] J.A. Shmerler, I. Mudawar, Local heat transfer coefficient in wavy free-falling turbulent liquid films undergoing uniform sensible heating, Int. J. Heat Mass Transfer 31 (1988) 67–77.
[7] J.A. Shmerler, I. Mudawar, Local evaporative heat transfer coefficient in turbulent free-falling liquid films, Int. J. Heat Mass Transfer 31 (1988) 731–742.
[8] T.H. Lyu, I. Mudawar, Statistical investigation of the relationship between interfacial waviness and sensible heat transfer to a falling liquid film, Int. J. Heat Mass Transfer 34 (1991) 1451–1464.
[9] T.H. Lyu, I. Mudawar, Determination of wave-induced fluctuations of wall temperature and convective heat transfer coefficient in the heating of a turbulent falling liquid film, Int. J. Heat Mass Transfer 34 (1991) 2521–2534.

[10] I. Mudawar, R.A. Houpt, Mass and momentum transport in Falling liquid films laminarized at relatively high Reynolds numbers, Int. J. Heat Mass Transfer 36 (1993) 3437–3448.
[11] I. Mudawar, R.A. Houpt, Measurement of mass and momentum transport in wavy-laminar falling liquid films, Int. J. Heat Mass Transfer 36 (1993) 4151–4162.
[12] I. Mudawar, M.A. El-Masri, Momentum and heat transfer across freely-falling turbulent liquid films, Int. J. Multiphase Flow 12 (1986) 771–790.
[13] S.M. Kim, I. Mudawar, Flow condensation in parallel micro-channels. Part 2: heat transfer results and correlation technique, Int. J. Heat Mass Transfer 55 (2012) 984–994.
[14] S.M. Kim, I. Mudawar, Analytical heat diffusion models for different micro-channel heat sink cross-sectional geometries, Int. J. Heat Mass Transfer 53 (2010) 4002–4016.
[15] J.E. Koskie, I. Mudawar, W.G. Tiederman, Parallel-wire probes for measurement of thick liquid films, Int. J. Multiphase Flow 15 (1989) 521–530.
[16] W. Qu, I. Mudawar, Transport phenomena in two-phase micro-channel heat sinks, ASME J. Electron. Packaging 126 (2004) 213–224.
[17] K.A. Triplett, S.M. Ghiaasiaan, S.I. Abdel-Khalik, D.L. Sadowski, Gas-liquid two-phase flow in microchannels. Part I: two-phase flow patterns, Int. J. Multiphase Flow 25 (1999) 377–394.
[18] P.M.-Y. Chung, M. Kawaji, The effect of channel diameter on adiabatic two-phase flow characteristics in microchannels, Int. J. Multiphase Flow 30 (2004) 735–761.
[19] H.M. Soliman, The mist-annular transition during condensation and its influence on the heat transfer mechanism, Int. J. Multiphase Flow 12 (1986) 277–288.
[20] Q. Chen, R.S. Amano, M. Xin, Experimental study of flow patterns and regimes of condensation in horizontal three-dimensional micro-fin tubes, Heat Mass Transfer 43 (2006) 201–206.
[21] J.G. Collier, J.R. Thome, Convective Boiling and Condensation, third ed., Oxford University Press, New York, 1994.
[22] G.E. Geiger, Sudden contraction losses in single and two-phase flow, Ph.D. Thesis, University of Pittsburgh, PA, 1964.
[23] W. Zhi-qing, Study on correction coefficients of laminar and turbulent entrance region effect in round pipe, Appl. Math. Mech. 3 (1982) 433–446.
[24] R.K. Shah, A.L. London, Laminar Flow Forced Convection in Ducts: A Source Book For Compact Heat Exchanger Analytical Data, Academic press, New York, 1978 (Supl 1).
[25] F.P. Incropera, D.P. Dewitt, Fundamentals of Heat and Mass Transfer, fifth ed., Wiley, New York, 2002.
[26] S.M. Zivi, Estimation of steady-state steam void-fraction by means of the principle of minimum entropy production, ASME J. Heat Transfer 86 (1964) 247–252.
[27] W.Y. Lewis, S.A. Robertson, The circulation of water and steam in water-tube boilers and the rational simplification of boiler design, in: Proc. Inst. Mech. Eng., London, vol. 143, 1940, pp. 147–181.
[28] A.A. Markson, T. Raverse, C.G.R. Humphreys, A method for estimating the circulation in steam boiler furnace circuits, Trans. ASME 64 (1942) 275–286.
[29] W.T. Bottomley, Flow of boiling water through orifices and pipes, Trans. North East Coast Inst. Eng. Ship Builders 53 (1936) 65–100.
[30] N.W. Benjamin, J.G. Miller, The flow of a flashing mixture of water and steam through pipes, Trans. ASME 64 (1942) 657–664.
[31] W.F. Allen, Flow of a flashing mixture of water and steam through pipes and valves, Trans. ASME 73 (1951) 257–265.
[32] W.H. McAdams, W.K. Woods, L.C. Heroman, Vaporization inside horizontal tubes. II: Benzene-oil mixture, Trans. ASME 64 (1942) 193–200.
[33] W.W. Akers, H.A. Deans, O.K. Crosser, Condensing heat transfer within horizontal tubes, Chem. Eng. Prog. 54 (1958) 89–90.
[34] A. Cicchitti, C. Lombardi, M. Silvestri, G. Soldaini, R. Zavalluilli, Two-phase cooling experiments-pressure drop, heat transfer and burnout measurements, Energ. Nucl. 7 (1960) 407–425.
[35] W.L. Owens, Two-phase pressure gradient, Int. Dev. Heat Transfer, Part II (1961).
[36] A.E. Dukler, M. Wicks, R.G. Cleaveland, Pressure drop and hold up in two-phase flow, AIChE J. 10 (1964) 38–51.
[37] D.R.H. Beattie, P.B. Whalley, A simple two-phase frictional pressure drop calculation method, Int. J. Multiphase Flow 8 (1982) 83–87.
[38] S. Lin, C.C.K. Kwok, R.Y. Li, Z.H. Chen, Z.Y. Chen, Local frictional pressure drop during vaporization of R-12 through capillary tubes, Int. J. Multiphase Flow 17 (1991) 95–102.
[39] R.W. Lockhart, R.C. Martinelli, Proposed correlation of data for isothermal two-phase, two-component flow in pipes, Chem. Eng. Prog. 45 (1949) 39–48.
[40] L. Friedel, Improved friction pressure drop correlations for horizontal and vertical two-phase pipe flow, European Two-phase Group Meeting, Ispra, Italy, 1979 Paper E2.
[41] D. Chisholm, Two-Phase Flow in Pipelines and Heat Exchanger, Longman, New York, 1983.
[42] H. Muller-Steinhagen, K. Heck, A simple friction pressure drop correlation for two-phase flow in pipes, Chem. Eng. Process. 20 (1986) 297–308.
[43] D.S. Jung, R. Radermacher, Prediction of pressure drop during horizontal annular flow boiling of pure and mixed refrigerants, Int. J. Heat Mass Transfer 32 (1989) 2435–2446.
[44] C.C. Wang, C.S. Chiang, D.C. Lu, Visual observation of two-phase flow pattern of R-22, R-134a, and R-407C in a 6.5-mm smooth tube, Exp. Thermal Fluid Sci. 15 (1997) 395–405.
[45] A. Cavallini, G. Censi, D.D. Col, L. Doretti, G.A. Longo, L. Rossetto, Condensation of halogenated refrigerants inside smooth tubes, HVAC&R Research 8 (2002) 429–451.
[46] K. Mishima, T. Hibiki, Some characteristics of air–water two-phase flow in small diameter vertical tubes, Int. J. Multiphase Flow 22 (1996) 703–712.
[47] T.N. Tran, M.-C. Chyu, M.W. Wambsganss, D.M. France, Two-phase pressure drop of refrigerants during flow boiling in small channels: an experimental investigation and correlation development, Int. J. Multiphase Flow 26 (2000) 1739–1754.
[48] H.J. Lee, S.Y. Lee, Pressure drop correlations for two-phase flow within horizontal rectangular channels with small heights, Int. J. Multiphase Flow 27 (2001) 783–796.
[49] M. Zhang, R.L. Webb, Correlation of two-phase friction for refrigerants in small-diameter tubes, Exp. Thermal Fluid Sci. 25 (2001) 131–139.
[50] I.Y. Chen, K.-S. Yang, Y.-J. Chang, C.-C. Wang, Two-phase pressure drop of air-water and R-410A in small horizontal tubes, Int. J. Multiphase Flow 27 (2001) 1293–1299.
[51] W. Yu, D.M. France, M.W. Wambsganss, J.R. Hull, Two-phase pressure drop, boiling heat transfer, and critical heat flux to water in a small-diameter horizontal tube, Int. J. Multiphase Flow 28 (2002) 927–941.
[52] V.G. Nino, E.W. Jassim, P.S. Hrnjak, T.A. Newell, Flow regime based model for pressure drop predictions in microchannels, University of Illinois at Urbana-Champaign, 2005 ACRC TR-242.
[53] J. Lee, I. Mudawar, Two-phase flow in high-heat-flux micro-channel heat sink for refrigeration cooling applications: Part I - pressure drop characteristics, Int. J. Heat Mass Transfer 48 (2005) 928–940.
[54] Y.W. Hwang, M.S. Kim, The pressure drop in microtubes and the correlation development, Int. J. Heat Mass Transfer 49 (2006) 1804–1812.